nature energy

ARTICLES

PUBLISHED: 14 AUGUST 2017 | VOLUME: 2 | ARTICLE NUMBER: 17135

Efficient ambient-air-stable solar cells with 2D–3D heterostructured butylammonium-caesium-formamidinium lead halide perovskites

Zhiping Wang, Qianqian Lin, Francis P. Chmiel, Nobuya Sakai, Laura M. Herz and Henry J. Snaith*

Perovskite solar cells are remarkably efficient; however, they are prone to degradation in water, oxygen and ultraviolet light. Cation engineering in 3D perovskite absorbers has led to reduced degradation. Alternatively, 2D Ruddlesden–Popper layered perovskites exhibit improved stability, but have not delivered efficient solar cells so far. Here, we introduce *n*-butylammonium cations into a mixed-cation lead mixed-halide $FA_{0.83}Cs_{0.17}Pb(I_yBr_{1-y})_3$ 3D perovskite. We observe the formation of 2D perovskite platelets, interspersed between highly orientated 3D perovskite grains, which suppress non-radiative charge recombination. We investigate the relationship between thin-film composition, crystal alignment and device performance. Solar cells with an optimal butylammonium content exhibit average stabilized power conversion efficiency of 17.5 ± 1.3% with a 1.61-eV-bandgap perovskite and 15.8 ± 0.8% with a 1.72-eV-bandgap perovskite. The stability under simulated sunlight is also enhanced. Cells sustain 80% of their 'post burn-in' efficiency after 1,000 h in air, and close to 4,000 h when encapsulated.

Organic–inorganic metal halide perovskites have emerged as one of the most promising next-generation photovoltaic materials due to their outstanding properties, such as tunable bandgap[1,2], long electron–hole diffusion lengths[3], low recombination rates[4] and low-temperature processability[5], which lead to the promise of both high efficiency and ultralow fabrication cost[6]. The small-laboratory-based cell efficiency has already reached a certified 22.1% (ref. 7), matching mainstream multi-crystalline silicon. Despite this achievement however, long-term stability suitable to deliver greater than 25 years of outdoor operation remains unproven.

Three-dimensional (3D) perovskite materials reported thus far, especially those based on the methylammonium (MA) cation, suffer from intrinsic instability and are prone to degradation following exposure to moisture, heat, oxygen and light[8–12]. The archetypal MA-based perovskite solar cells (that is, methylammonium lead triiodide: $MAPbI_3$) exhibit intrinsic thermal instability due to the relatively volatile MA cations, which are released from the film during heating, and this process is accelerated in the presence of moisture[12–14]. In addition, oxygen radical formation appears to be a key driver for solar cell degradation due to a reaction with methyl ammonium[9,11]. We have previously shown that formamidinium (FA)-based perovskites exhibit much greater thermal stability than MA-based perovskites[8,15]. Furthermore, $FAPbI_3$ can be stabilized in the required black α-phase, by the partial substitution of FA with caesium (Cs) cations, to form a thermally and structurally stable perovskite[15–17].

In addition to developing resilient 3D perovskite materials, another approach to improving device stability is to employ 2D Ruddlesden–Popper phase layered perovskites (that is, $(RNH_3)_2(A)_{n-1}BX_{3n+1}$), where RNH_3 are large alkyl ammonium cations. The RNH_3 cations act as a spacer between the lead halide octahedral perovskite planes, and the A, B and X ions forming the perovskite framework[18,19]. These 2D phases have shown superior moisture stability over solely 3D methylammonium-based perovskites[20,21]. However, until recently, perovskite solar cells employing layered perovskite compounds have exhibited relatively low efficiency (PCE < 10%) (refs 20,22), assumed to be due to the inhibition of out-of-plane charge transport by the insulating spacer cations. A recent study adopted a 'hot-casting' technique to fabricate highly crystalline $(BA)_2(MA)_3Pb_4I_{13}$ (BA: *n*-butylammonium, $C_4H_9NH_3$) Ruddlesden–Popper phase perovskite films with the crystalline planes aligned along the out-of-plane orientation, which facilitates efficient charge transport along the perovskite planes, achieving a 12.5%-efficient layered perovskite solar cell with improved moisture and light stability[23]. Despite the significantly enhanced stability, the application of 2D perovskites in photovoltaics is limited by their short carrier diffusion length, low carrier mobility and narrower absorption windows[18,20,21,24,25]. More recent efforts involving 2D perovskites has been focused on tuning the '*n*' values, that is, the number of planes of the corner-sharing lead halide octahedral between each RNH_3 plane[24,26–28]. However, the enhanced air stability has thus far been at the cost of the solar cell efficiency.

Herein, we incorporate butylammonium, within the caesium-formamidinium lead halide perovskite. We observe 'plate-like' 2D-phase crystallites standing up between the 3D perovskite grains, and remarkably enhanced crystallinity. We observe inhibition of non-radiative recombination within this 'heterostructured' film, which we postulate to be due to interfacial grain boundary passivation. In complete solar cells, we achieved a champion stabilized efficiency of 19.5% with a 1.61-eV-bandgap perovskite and 17.3% employing a 1.72-eV-bandgap perovskite. Additionally, we observe greatly enhanced stability under simulated sunlight, with cells sustaining 80% of their 'post burn-in' efficiency after 1,000 h in air, and close to 4,000 h when encapsulated. Our work illustrates that engineering heterostructures between 2D and 3D perovskite phases is possible, and can lead to enhancement of both performance and stability of perovskite solar cells.

BA/FA/Cs crystallized perovskite thin films

Our perovskite films are based on the mixed-cation lead mixed-halide $FA_{0.83}Cs_{0.17}Pb(I_{0.6}Br_{0.4})_3$ composition unless otherwise

Clarendon Laboratory, Department of Physics, University of Oxford, Parks Road, Oxford OX1 3PU, UK. *e-mail: henry.snaith@physics.ox.ac.uk

stated. We tune the BA-to-FA/Cs mixing ratio by substituting different amounts of FA/Cs (fixed at a molar ratio of 0.83:0.17 in the starting solution) with BA cations. We tested a series of $BA_x(FA_{0.83}Cs_{0.17})_{1-x}Pb(I_{0.6}Br_{0.4})_3$ precursor compositions from $x = 0$ (that is, pristine $FA_{0.83}Cs_{0.17}Pb(I_{0.6}Br_{0.4})_3$) to $x = 1$, and the molar ratio of $BA_x(FA_{0.83}Cs_{0.17})_{1-x}$ to $Pb(I_{0.6}Br_{0.4})_3$ is kept at 1:1. We observe some changes to the as-cast pre-crystallized films with the addition of BA, which we show and discuss in Supplementary Figs 1 and 2. To obtain the fully crystallized perovskite films, we anneal the precursor films at 175 °C for 80 min in air. We first assess if there is any morphological change following BA incorporation. In Fig. 1, we show scanning electron microscope (SEM) images of perovskite films with different BA concentrations. The pristine FA/Cs perovskite film (that is, $x = 0$) displays a dense, pinhole-free morphology with 2- to 5-μm-size grains. By substituting 3% FA/Cs with BA (that is, $x = 0.03$), we observe an increase in the average grain size, coexisting with the emergence of 'plate-like' crystallites (Fig. 1g). By further increasing the BA content to $x = 0.09$ and 0.16, we observe a higher density of these plate-like crystallites, which appear to be interspersed between the larger 'flat' grains. With further addition of BA, the average grain size appears to shrink again.

To study the crystal structure of the perovskite films, we perform 2D X-ray diffraction (2D-XRD) measurements[29]. In Fig. 1a (insets), we show 2D-XRD images of perovskite films with different BA concentrations. In the $x = 0$ film, we assign all reflections to either the 3D $FA_{0.83}Cs_{0.17}Pb(I_{0.6}Br_{0.4})_3$ perovskite (in the primitive cubic setting; $a = b = c = 6.22$ Å, $\alpha = \beta = \gamma = 90°$) (ref. 15) or the polycrystalline FTO substrate; we show the $2\theta/\omega$ scan in Supplementary Fig. 3. We determine from the 2D-XRD data that in the $x = 0$ film the 3D perovskite phase displays some degree of texture compared with the archetypal $CH_3NH_3PbI_3$ perovskite[15,30]. With the introduction of BA, we observe a significant further increase in the peak intensities of the (h00) reflections in the 2D-XRD scans and a disappearance of the powder diffraction rings, indicative of a much greater preference for the [100] direction to align parallel to the substrate normal. Furthermore, in the specular $2\theta/\omega$ scan (Supplementary Fig. 3), the peak intensities of the (h00) reflections increase by a factor of 10 and all other (hkl) reflections disappear. We also observe additional reflections as we increase the BA concentration, in particular several off-specular reflections arise, which we mark with white arrows in Fig. 1c–e insets. As the BA content increases further, new reflections arise that we mark with red arrows in the insets to Fig. 1e,f, whilst the reflections marked with the white arrows disappear. These reflections cannot arise from the orientated 3D perovskite, since they are too low in 2θ and too close to the specular direction. They therefore arise from additional phases with larger d-spacing than the 3D perovskite. The phases responsible for these lower angle reflections are also notably orientated, since we do not observe powder diffraction rings. These new reflections are coincident with the appearance of the plate-like structures, which we observed in the SEM images. We thus assign the additional reflections to these structures. Since BA is known to form layered perovskite phases when mixed with MA in $(BA)_2(MA)_{n-1}PbI_{3n+1}$, we assume that the platelets we observe here are composed of $(BA)_2(FA_{0.83}Cs_{0.17})_{n-1}Pb(I_{0.6}Br_{0.4})_{3n+1}$ phases, probably orientated with their longest crystallographic axis in the sample plane[23,31]. We cannot however assign the precise n-value, or composition of n-values, from our 2D-XRD data, due to the low scattering volume of these platelets and the likelihood of multiple phases (that is, a mixture of different 'n' values). The transition from the white-arrow-indicated to red-arrow-indicated reflections appears to coincide with the platelets lying down in the plane of the film. Therefore, the difference between these reflections could be either orientation, or an evolution of layered phases.

To further assess the orientation of the crystalline grains within the films, known as mosaicity[32,33], we measure rocking curves of the (200) reflections of the 3D perovskite phase, which we show in Fig. 2a. Whereas a $2\theta/\omega$ scan primarily characterizes the crystallographic phases, their d-spacing and associated lattice strain, a rocking curve is the most reliable measure of the average orientation of a particular crystallographic phase. For example, the full-width at half-maximum (FWHM) of a rocking curve (ω scan) is a direct measure of the deviation of the crystallographic grains from their average orientation. In a polycrystalline film with completely random grain orientation the FHWM would be undefined, and for a perfectly orientated single crystal it would be zero (ignoring instrument resolution limits). For our control perovskite film (that is, $x = 0$), we cannot determine a precise rocking curve, which is consistent with a polycrystalline film with a low degree of texture. In contrast, all of the films crystallized with the addition of BA clearly show resolvable rocking curves, with the (200) FWHM reduced to a minimum value of 3.3° at $x = 0.09$. This low value implies that the FA/Cs 3D perovskite phase greatly favours the orientation of the [100] direction parallel to the film normal (equivalently described as a preference for the (h00) planes to be parallel with the sample plane) when crystallizing in the presence of BA.

The well-defined surface-normal direction [100] of the $x = 0.09$ film allows us to investigate the 3D perovskite crystal orientation within the sample plane by performing a pole figure measurement of the (410) reflection[34], which we show in Fig. 2b. We observe a continuous ring of intensity as the sample is rotated about the [100] direction, indicating that there is no preferential orientation of the crystal grains within the sample plane. This result, along with the rocking curve of the $x = 0.09$ film, allows us to fully describe the orientation of the 3D perovskite phase as fully disordered within the sample plane but a high preference for the [100] direction to be aligned parallel to the film normal, which we illustrate in Fig. 2c. To investigate the mechanism driving the increased crystallinity and orientation of the perovskite grains with addition of BA, we further monitor the peak intensity of the (100) reflection as a function of time during annealing, for the $x = 0$ and $x = 0.09$ films; we show the data in Fig. 2d. The crystallization in the films in the presence of BA accelerates, and evolves to a much higher degree of crystallinity, the mechanism of which we will discuss later.

In addition to improving the crystallinity, the modification of the thin-film growth might also induce changes in the lattice parameter of the 3D perovskite phase. To obtain the lattice constant, we used least-squares refinement of a Lorentzian profile to fit the (100) Bragg reflection of the 3D perovskite, as we show in Supplementary Fig. 4a. In Supplementary Fig. 4b, we clearly observe that the lattice constant of the 3D perovskite decreases with increasing BA content; decreasing from $a = 6.22$ Å to 6.18 Å (∼0.6%). Changes in lattice constant can result from incorporation of foreign ions (that is, BA cations in this work), changes in the strain or changes in halide composition. In the case of FA/Cs substituted by BA in the 3D perovskite crystal structure, we would expect an increase in the lattice constant due to the larger ionic radius of BA. Additionally, due to its much larger size, we would not expect BA to be able to be incorporated within the 3D perovskite structure[35,36]. Therefore, the reduced lattice constant could be either due to a change in the lattice strain, potentially due to the 3D perovskite grains interfacing with the layered phases, or simply released strain due to the significant reduction in the mosaicity of the film. Alternatively, the reduced lattice constant may be due to the precise I/Br composition in the crystallized perovskite film varying with the BA addition, possibly imposed by the change in crystallization kinetics. We note that we fix the total Br to I composition in the starting solution at 0.4 to 0.6. However, we do not know the precise final composition in the crystallized films. We also note that a lattice contraction of 0.6% is consistent with a change in Br/I composition from 0.4/0.6 to 0.43/0.57, and we would expect a corresponding bandgap reduction of 30 meV (ref. 15).

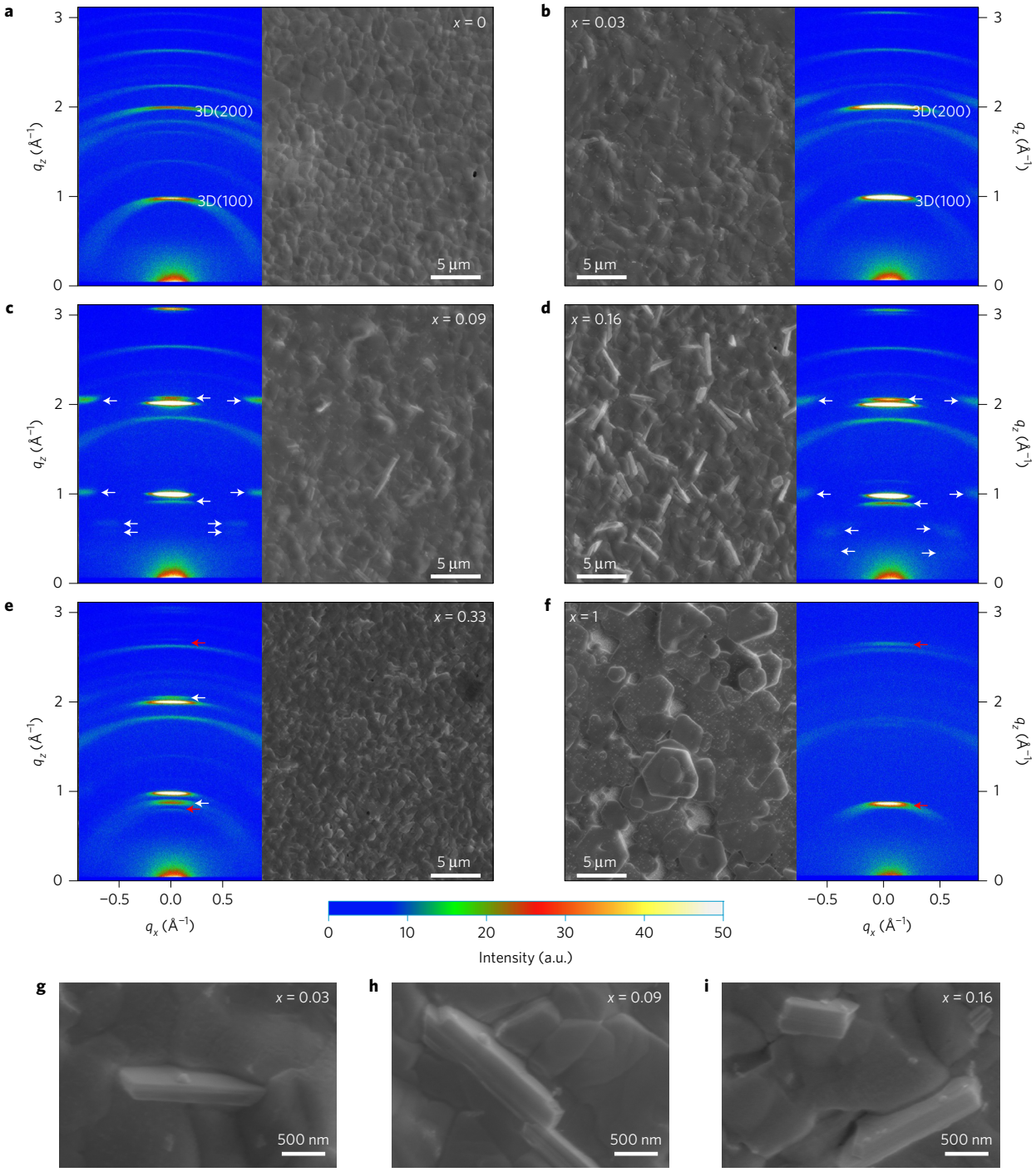

Figure 1 | Morphology and crystal phases. a–f, SEM images of post-annealed $BA_x(FA_{0.83}Cs_{0.17})_{1-x}Pb(I_{0.6}Br_{0.4})_3$ perovskite films with different BA concentrations, grown on FTO/SnO_2/fullerene C_{60} substrates. The insets show 2D-XRD images of the films of different BA concentrations. Reflections at $q_z \approx 1$ and 2 Å^{-1} are assigned to 3D perovskite (100) and (200), respectively. The white arrows in the 2D-XRD images highlight new diffraction peaks that appear at low BA content, and the red arrows highlight diffraction peaks that arise at higher BA contents. **g–i**, Enlarged SEM images of x = 0.03, 0.09 and 0.16 films.

To investigate whether the plate-like features extend throughout the film, we show cross-sectional SEM images of the x = 0 and x = 0.09 perovskite films incorporated into complete photovoltaic devices in Fig. 3a,b. We observe some thin crystals, vertically aligned in the x = 0.09 film. These crystals are of similar size and width to the platelets we observe in the surface-view SEM images (Fig. 1), consistent with these platelets being preferentially orientated in the perpendicular direction to the substrate. This additional information allows us to form a clear understanding of the role of BA in the crystallization of the FA/Cs perovskite film. The BA cations expel from the crystallizing 3D perovskite domains as crystallization proceeds, but appear to act as a flux, accelerating crystal growth. Since the 3D domains are preferentially aligned with the (010) plane perpendicular to the plane of the substrate, the most favourable means by which the 2D perovskite phase can interface well with the 3D perovskite phase, without a significant energetic cost, is to also align with their (010) plane perpendicular to the plane of the substrate. We illustrate such a 2D/3D crystal interface

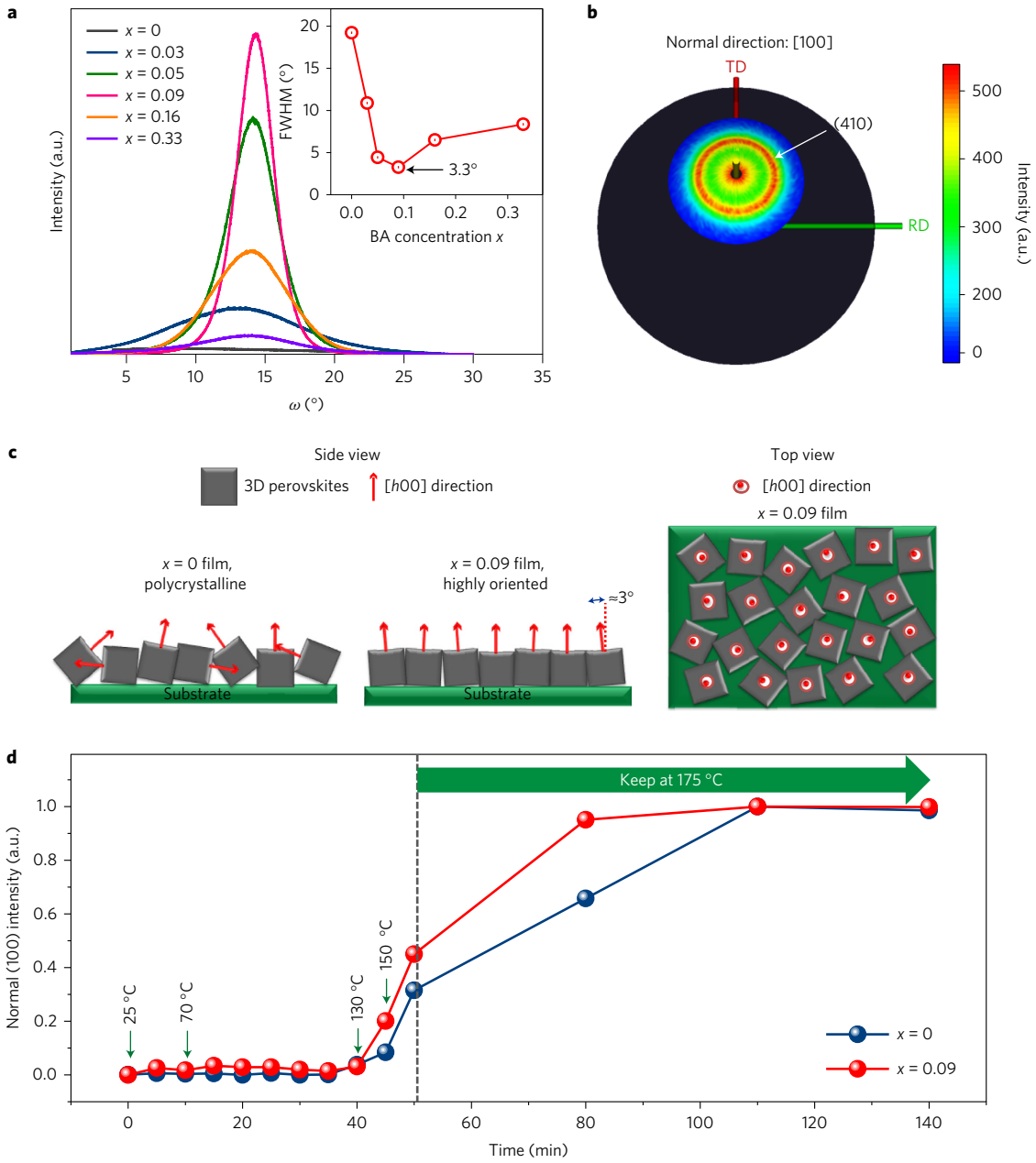

Figure 2 | BA-enhanced 3D perovskite crystalline growth. a, XRD rocking curves of the 3D perovskite (200) reflections with varying BA concentrations. The inset shows the FWHM values of the rocking curves. **b**, Pole figure of the (410) reflection of the 3D perovskite phase in the $x = 0.09$ film. RD and TD represent rolling direction and transverse direction, respectively, within the plane. The [100] direction defines the surface-normal direction. **c**, Illustration, depicting the orientation of the 3D perovskite phase in the $x = 0.09$ film, compared with a low-textured $x = 0$ film, showing a preference for the [*h*00] direction to align out-of-plane and no preferential orientation within the plane. Note that these squares just schematically illustrate the crystal orientation rather than the crystal grains. The real grains impinge together forming a dense, pinhole-free morphology as we observed in the SEM images. **d**, Intensity of (100) reflection as a function of time during the perovskite annealing procedure (from room temperature to 175 °C) for two different BA concentrations ($x = 0$ and 0.09).

in Fig. 3c. Since the lattice constant in the plane of the lead halide sheet of the layered perovskite phase is very close to the lattice constant in the 3D perovskite phase, there is a good possibility that lattice matching will occur between these phases, which could be electronically advantageous. We also note that since the halides, FA and Cs cations are relatively diffusive within the perovskite films, it will be feasible for the precise mixed A-site and halide compositions to be dissimilar within the 3D and 2D phases, which should facilitate reduced strain and easier lattice matching. With the 100% BA, the grains appear to lie flat in the plane of the film, and at some critical concentration at around $x = 0.33$, the platelet features appear to preferentially lay down. This change in orientation of the platelets is likely to reduce the surface energy of the film, once the concentration of platelets exceeds a certain threshold.

To assess whether this compositionally 'heterogeneous' film is advantageous or disadvantageous concerning light absorption and charge recombination, in Fig. 3d,e we present ultraviolet–visible absorption and photoluminescence (PL) spectra, and time-resolved PL traces for the post-annealed films. With the introduction of BA, we observe a slight blueshift in the PL position, consistent with the slight shrinkage of the 3D crystal lattice. We also observe significant increases in the PL lifetime of the perovskite

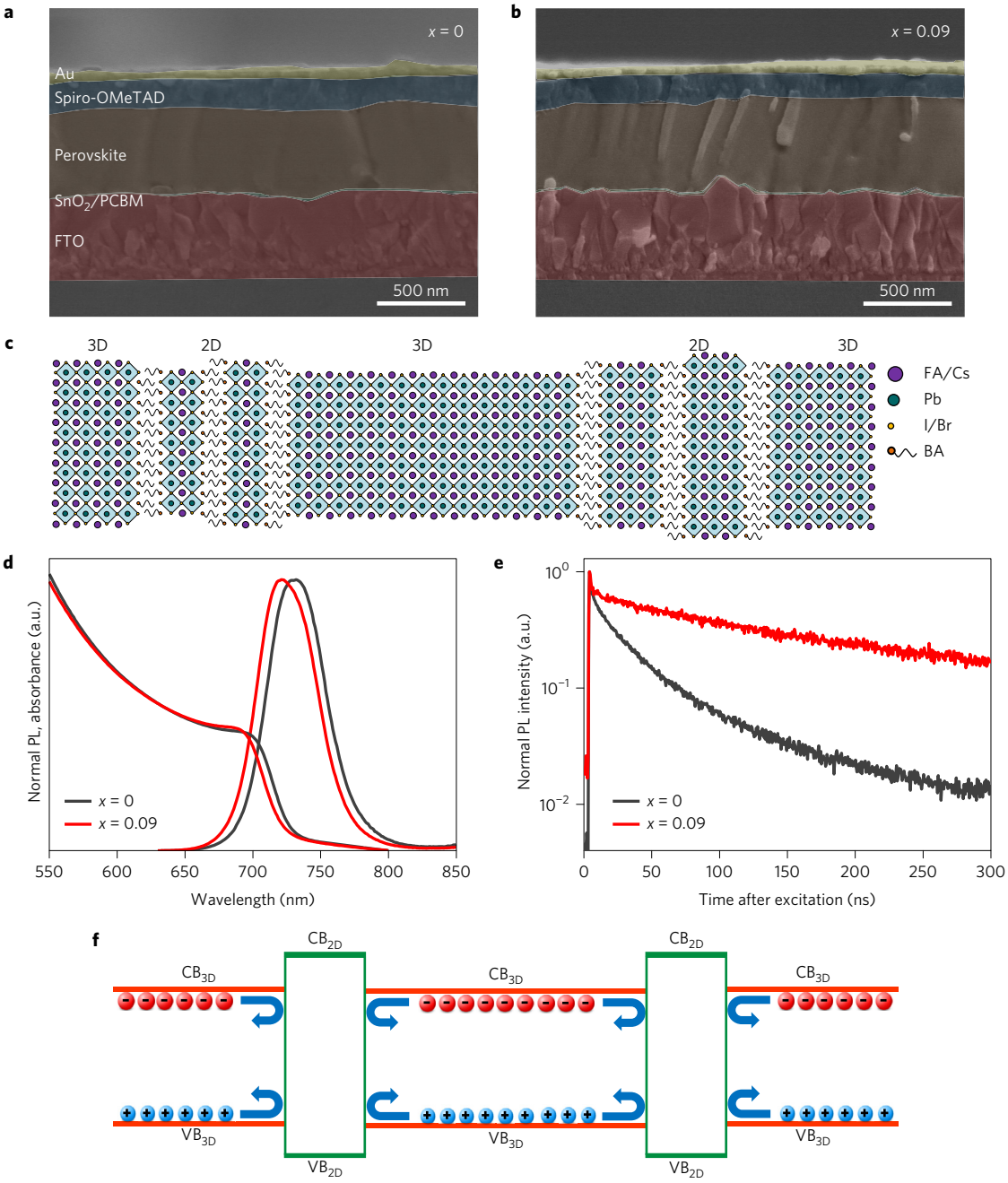

Figure 3 | 2D–3D perovskite heterostructure. a,**b**, Cross-sectional SEM images with artificial colour of $FA_{0.83}Cs_{0.17}Pb(I_{0.6}Br_{0.4})_3$ ($x = 0$) (**a**) and $BA_{0.09}(FA_{0.83}Cs_{0.17})_{0.91}Pb(I_{0.6}Br_{0.4})_3$ ($x = 0.09$) (**b**) complete photovoltaic devices. The solar cell materials stack from bottom to top is glass/FTO/SnO_2/$PC_{61}BM$/perovskite/spiro-OMeTAD/Au, as detailed in **a**. **c**, Schematic illustration of the proposed self-assembled 2D–3D perovskite film structure. **d**, Ultraviolet–visible absorption and PL spectra of an $x = 0$ film (black line) and an $x = 0.09$ film (red line). **e**, Time-resolved PL spectra for the same films. **f**, Proposed electronic band offsets of the 2D–3D heterojunction. CB and VB stand for conduction band and valence band, respectively, with the subscript indicating either the 2D or 3D phase.

films incorporating BA, consistent with a significant reduction in non-radiative recombination in the films. This reveals that the presence of the 2D platelets suppresses charge recombination.

With the above observations, we postulate that the 2D perovskite phases interface with the 3D phases at what would have otherwise been grain boundaries. Since this heterojunction between 2D and 3D phases inhibits charge recombination, we assume that the crystallographic connectivity between the two phases is good, without a significant density of crystal defects, and hence presents a clean electronic interface. Since the bandgaps of the layered perovskite phases are wider than the bandgap of the 3D phases[37], the electronic configuration across the 2D–3D heterojunction will be similar to a classical type-I or type-II heterojunction[38]. We illustrate such a type-I configuration in Fig. 3f. Therefore, when charges reach this interface from within the 3D grain, they will be reflected remaining in the 3D perovskite and not suffer from trapping and recombination at the grain boundaries.

Photovoltaic performance

To assess whether the BA/FA/Cs perovskite can enhance the solar cell performance, we fabricate devices based on a negative–intrinsic–positive (n–i–p) planar heterojunction architecture.

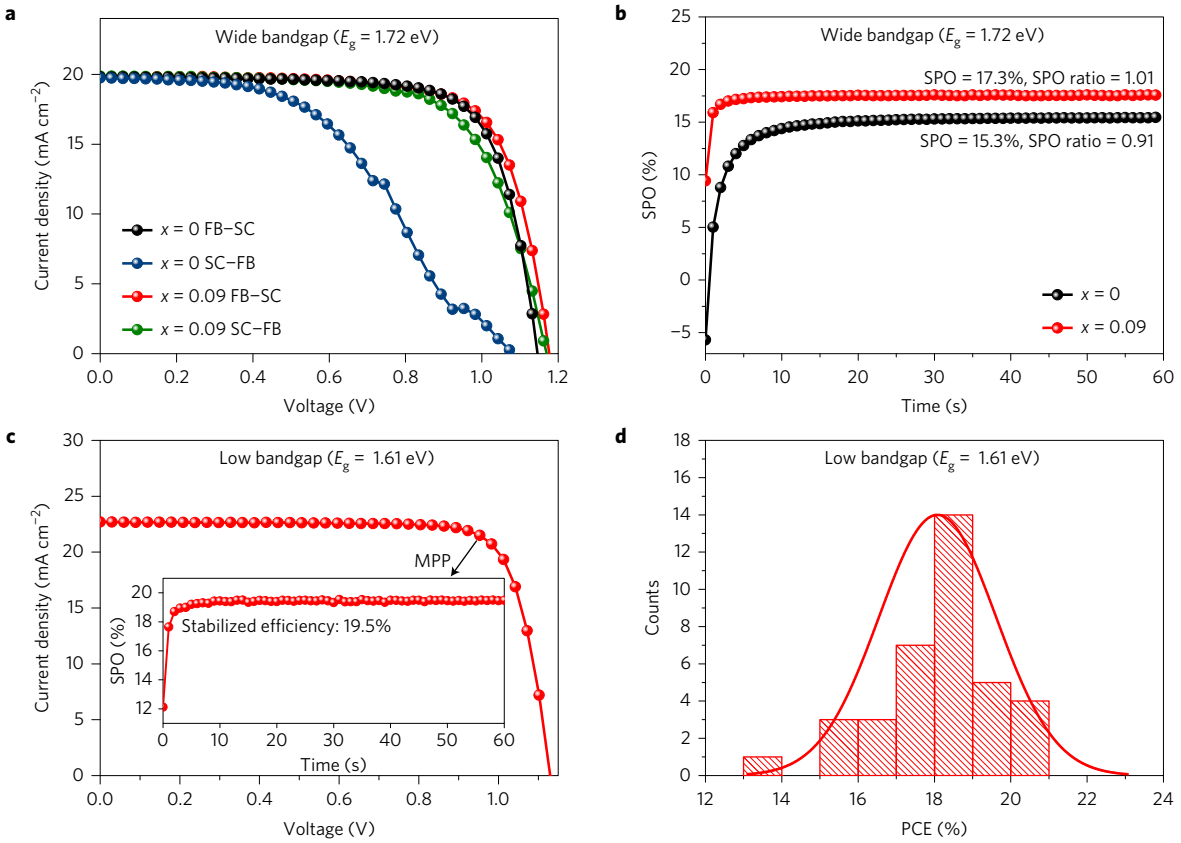

Figure 4 | Device performances of the BA/FA/Cs perovskite solar cells. a, *J*–*V* curves for perovskite solar cells using the wide-bandgap (E_g = 1.72 eV) $FA_{0.83}Cs_{0.17}Pb(I_{0.6}Br_{0.4})_3$ (labelled as *x* = 0) and $BA_{0.09}(FA_{0.83}Cs_{0.17})_{0.91}Pb(I_{0.6}Br_{0.4})_3$ (labelled as *x* = 0.09) perovskite active layers, measured from forward bias (FB) to short-circuit (SC) and back again with a scan rate of 380 mV s^{-1}. **b**, Stabilized power output (SPO) of the champion cells, determined by holding the cell at a fixed voltage near the maximum power point (MPP) on the *J*–*V* curve for 60 s. The SPO ratio is the ratio between the SPO and the efficiency determined from the FB–SC *J*–*V* scan of the same cell. **c**, *J*–*V* characteristic of a best-performing perovskite solar cell using a lower-bandgap (E_g = 1.61 eV) $BA_{0.05}(FA_{0.83}Cs_{0.17})_{0.95}Pb(I_{0.8}Br_{0.2})_3$ active layer; the inset shows the corresponding SPO data. The cell structure for both the wide- and low-bandgap perovskite devices is glass/FTO/SnO_2/PC_{61}BM/perovskite/spiro-OMeTAD (with Li-TFSI and *t*BP additives)/Au. The cells are measured under simulated AM1.5G solar irradiance at 100 mW cm^{-2}. The bandgaps are determined from Tauc plots of the absorption spectra and inflection points of EQE spectra, shown in Supplementary Fig. 10. **d**, Histogram of the number of cells as a function of PCE of $BA_{0.05}(FA_{0.83}Cs_{0.17})_{0.95}Pb(I_{0.8}Br_{0.2})_3$ perovskite devices. The curve is a normal distribution function, illustrating the spread in measured performance.

Table 1 | Solar cell performance parameters determined from *J*–*V* curves and stabilized power output measurements.

Device	PCE (%)	J_{sc} (mA cm^{-2})	V_{oc} (V)	FF	SPO (%)
Wide-bandgap $FA_{0.83}Cs_{0.17}Pb(I_{0.6}Br_{0.4})_3$ (*x* = 0)					
Average	15.1 ± 1.0	18.8 ± 0.9	1.15 ± 0.02	0.70 ± 0.03	14.1 ± 0.9
Champion	16.9	19.8	1.14	0.75	15.3
Wide-bandgap $BA_{0.09}(FA_{0.83}Cs_{0.17})_{0.91}Pb(I_{0.6}Br_{0.4})_3$ (*x* = 0.09)					
Average	15.5 ± 1.1	18.9 ± 0.7	1.17 ± 0.02	0.70 ± 0.04	15.8 ± 0.8
Champion	17.2	19.8	1.18	0.73	17.3
Low-bandgap $BA_{0.05}(FA_{0.83}Cs_{0.17})_{0.91}Pb(I_{0.8}Br_{0.2})_3$					
Average	18.1 ± 1.5	22.1 ± 0.7	1.09 ± 0.04	0.75 ± 0.05	17.5 ± 1.3
Champion	20.6	22.7	1.14	0.80	19.5

Average device characteristics with standard deviation were obtained on the basis of 32 cells for each set. The champion cell data are taken from the *J*–*V* curves shown in Fig. 4.

In Fig. 4a, we show current density voltage (*J*–*V*) characteristics of champion devices, measured under simulated sunlight, and give the full performance parameters in Table 1 and Supplementary Figs 5 and 6, and a typical external quantum efficiency (EQE) spectrum in Supplementary Fig. 7. The champion BA/FA/Cs perovskite device, with a perovskite bandgap of 1.72 eV, exhibits a short-circuit current (J_{sc}) of 19.8 mA cm^{-2}, a fill factor (FF) of 0.73, and an open-circuit voltage (V_{oc}) of 1.18 V, yielding a PCE of 17.2%. The control device (that is, *x* = 0) exhibits significant *J*–*V* hysteresis, which is significantly reduced for the BA/FA/Cs device. Anomalous hysteresis is mainly caused by the migration of ionic species to the grain boundaries and perovskite thin-film interfaces, which subsequently modulate the trap-assisted, or surface recombination[39,40]. To gain a better understanding of the

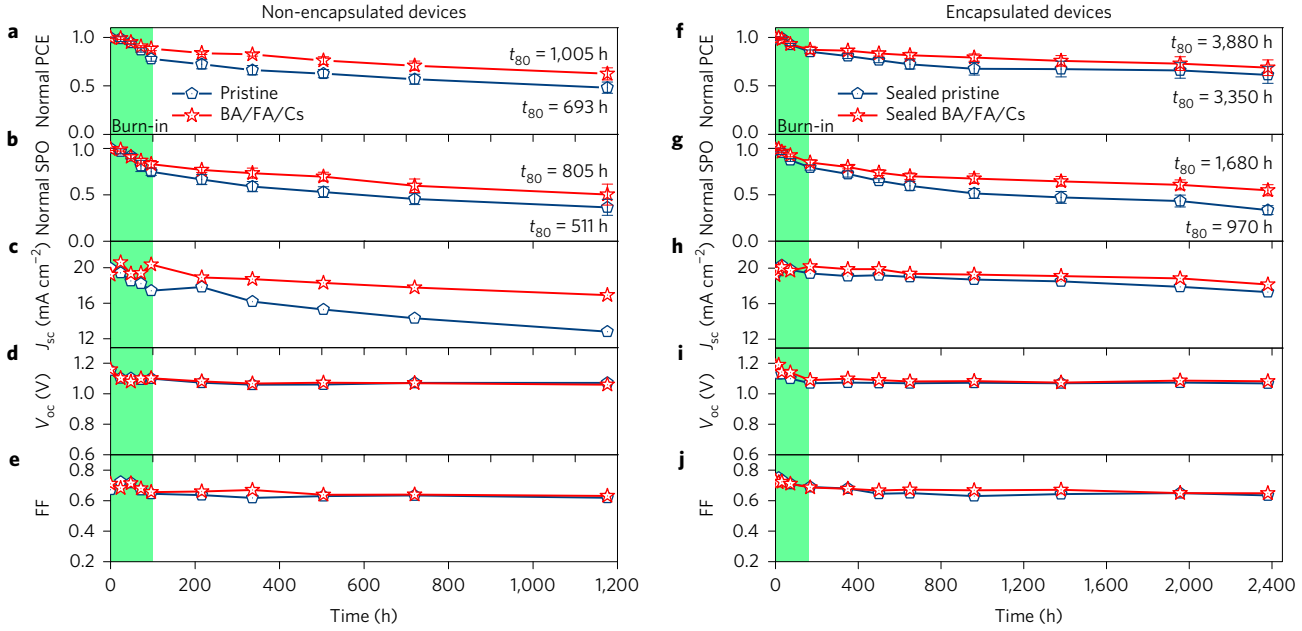

Figure 5 | Device stability. a–j, Comparison of stability of high-performance non-encapsulated (**a**–**e**) and encapsulated (**f**–**j**) solar cell devices using $FA_{0.83}Cs_{0.17}Pb(I_{0.6}Br_{0.4})_3$ (navy blue lines; labelled as pristine) and $BA_{0.09}(FA_{0.83}Cs_{0.17})_{0.91}Pb(I_{0.6}Br_{0.4})_3$ (red lines; labelled as BA/FA/Cs) perovskite active layers. The devices are aged under xenon-lamp simulated full-spectrum AM1.5, 76 mW cm^{-2} equivalent irradiance in air (humidity ~45 RH%) without any ultraviolet filter, held at open-circuit during ageing, and tested at different time intervals under a separate AM1.5 100 mW cm^{-2} solar simulator. The Suntest XLS+ ageing box irradiates pulsed light. There is an early burn-in with an exponential decay over the first ~100 h followed by an approximate linear decay. In the decay of PCE (**a**,**f**) and SPO (**b**,**g**), each average (symbol) and standard deviation (error bar) was calculated from eight devices. The evolution of J_{sc} (**c**,**h**), V_{oc} (**d**,**i**) and FF (**e**,**j**) is shown for the champion devices. The time to 80% of the post burn-in decay (t_{80}) of champion devices is shown on the graph (with the t_0 efficiency extrapolated back to the *y* axis from the linear fit, as shown in Supplementary Figs 12 and 13). The cell structure is glass/FTO/SnO_2/C_{60}/perovskite/spiro-OMeTAD (with Li-TFSI and *t*BP additives)/Au.

reduced hysteresis, we determine the stabilized power output (SPO)[41] by measuring the current at a fixed maximum power point (MPP) voltage over 60 s, which we show in Fig. 4b. Under constant operation, the efficiency of the control device rises over 15 s to reach a stabilized value of 15.2% with an SPO-to-PCE ratio (SPO ratio) of 0.91. In contrast, the x = 0.09 device stabilizes within 5 s at a higher value of 17.3%, yielding an SPO ratio of 1.01. The faster stabilizing rate and the higher SPO ratio is consistent with the perovskite film having a lower density of trap sites responsible for trap-assisted recombination[42], consistent with our measured enhancement in the PL lifetime. For polycrystalline perovskite solar cells, minimizing the charge recombination at grain boundaries is likely to be of great importance in reducing device hysteresis[43]. It appears that the presence of the 2D–3D heterostructure within these films has successfully alleviated hysteresis.

By employing a narrower-bandgap $BA_{0.05}(FA_{0.83}Cs_{0.17})_{0.95}Pb(I_{0.8}Br_{0.2})_3$ perovskite as the photoactive layer, we achieve a champion J–V measured PCE of 20.6%, and an SPO of 19.5%. We show the JV curves in Fig. 4c along with the photovoltaic performance parameters in Table 1 and the efficiency distribution in Fig. 4d. We also show further performance statistics and the EQE spectrum in Supplementary Figs 8 and 9 respectively.

As an aside, we have previously found that the FA/Cs-based perovskites require spin-coating in a nitrogen-filled glove box to achieve smooth and uniform films. Here, we find that the perovskite films incorporating BA can be processed in air under ambient humidity and the solar cells entirely fabricated in air operate reasonably well, as we show in Supplementary Fig. 11.

Device stability

To examine whether the BA/FA/Cs perovskite has an impact on device stability we perform ageing tests of high-performance non-encapsulated and encapsulated perovskite devices based on the wide-bandgap (1.72 eV) $FA_{0.83}Cs_{0.17}Pb(I_{0.6}Br_{0.4})_3$ perovskite under full-spectrum simulated sunlight. We note that we employ SnO_2/C_{60} as an electron-transporting layer for the stability test, although there is a slight improvement in the 'as fabricated' efficiency when employing SnO_2/$PC_{61}BM$. We show the ageing results in Fig. 5. We observe that the BA/FA/Cs non-encapsulated devices exhibit enhanced long-term stability, in comparison with the control FA/Cs device in both the J–V PCE and the SPO. This improvement primarily arises from the retarded J_{sc} decay. To perform a quantitative analysis, we fit the post 'burn-in' section of the PCE to a straight line and extrapolate the curve back to zero time to obtain the t = 0 efficiency[10]. We determine the lifetime to 80% degradation (t_{80}) from this t = 0 post burn-in efficiency[44] for the most stable BA/FA/Cs devices to be 1,005 h, and the SPO t_{80} lifetime is 805 h. This is nearly 50% longer than the t_{80} lifetime of the control FA/Cs device[10], and the surpassing of 1,000 h stability for an unsealed perovskite cell under these conditions marks a clear milestone in the progress towards perovskite solar cells and modules with industrially acceptable stability. We further proceed to encapsulate the devices with a hot-melt polymer foil and a glass coverslip and show the stability results in Fig. 5b. For the BA/FA/Cs perovskite devices, we achieve a champion t_{80} lifetime of 3,880 h for the J–V-measured PCE and 1,680 h for the SPO. We note that the control FA/Cs devices exhibit a champion t_{80} lifetime of 3,350 h, which is very close to the value for the BA/FA/Cs device. In contrast, the control SPO t_{80} lifetime of the encapsulated FA/Cs device is only 970 h, which is 40% lower than the BA/FA/Cs device. We note that the observation of a faster decay in the SPO versus measured PCE is consistent with an increase in the density of defects responsible for trap-assisted recombination occurring during ageing. Following from our understanding of J–V hysteresis, the scanned efficiency is insensitive to small changes in the density of defects responsible for trap-assisted recombination, because

electronic biasing during the measurements results in ion migration, which favourably stabilizes trapped charge at the charge collection interfaces. On the other hand, under steady-state operation near MPP the ions redistribute and the degree of favourable trap passivation is reduced, making the SPO more sensitive to increases in trap densities. Hence, we can infer that the defects form faster in the control devices absent of BA. Our results demonstrate a near doubling of the long-term stability in a like-to-like comparison with the control, FA/Cs cells, which were previously the most stable perovskite composition[10,15,45].

We believe that there are key advancements in BA/FA/Cs perovskite that contribute to the enhanced stability. Firstly, the introduction of the BA cations greatly improves the overall crystallinity in the material, indicative of a reduced number of crystal defects. The degradation of the perovskite films is likely to proceed via active defects[46] and hence reducing the number of defects is very likely to positively improve the long-term stability. Secondly, the presence of the layered perovskite phases at the grain boundaries is likely to inhibit degradation proceeding via the grain boundaries. A recent study suggested that the moisture-induced degradation of 3D perovskite films starts from grain boundaries[47]. Therefore, 'coating' 3D perovskite grains with either stable layered perovskite crystallites, or simply a shell of butylammonium, will help to protect the perovskite film from moisture, directly contributing to the stability enhancement.

Conclusion

In conclusion, we have demonstrated a perovskite composition exhibiting significantly improved device efficiency and operational stability. By carefully regulating the BA content, we obtain plate-like 'layered' perovskite crystallites orientated perpendicularly to the plane of the film, embedded between 3D perovskite grains. With this unique heterostructure, we observe greatly enhanced crystallinity and evidence for reduced defects responsible for non-radiative recombination, which leads to reduced current–voltage hysteresis, enhanced efficiency and significantly improved operational stability in the ensuing solar cells. Our work represents a significant step towards highly efficient perovskite solar cells having long-term operational stability commensurate with real-world outdoor applications. Equally importantly, we have demonstrated that it is possible to create stable heterostructures within a perovskite film, comprised of 3D and 2D domains. The interface between these heterostructures appears to be electronically clean, and consequently inhibits unwanted trap-assisted recombination. We note that type-I and type-II heterostructures have been central to controlling surface recombination in III–V semiconductor devices, such as GaAs photovoltaics and GaN light-emitting diodes. Our findings open the possibility of developing much more controlled 2D–3D perovskite heterostructures, and investigating the optoelectronic processes occurring at these interfaces. We believe that this will prove to be an important direction for ongoing developments in perovskite solar cells and optoelectronic devices, and may deliver model systems for fundamental investigations.

Methods

Preparation of perovskite precursor. *Formamidinium iodide synthesis.* $HC(NH_2)_2I$ (formamidinium iodide, FAI) was synthesized by dissolving formamidine acetate (Sigma-Aldrich) powder in a 1.5 M excess of hydroiodic acid (HI; Sigma-Aldrich), 57 wt% in H_2O. After addition of the acid, the solution was stirred for 10 min at 50 °C. After drying at 100 °C for approximately 2 h, a yellow-white powder is formed. This powder was then washed three times with diethyl ether to remove excess I_2. The powder was later dissolved in ethanol and heated at 80 °C to obtain a supersaturate solution. Once fully dissolved, the solution was then placed in a refrigerator overnight for recrystallization. The recrystallization process formed white flake-like crystals. The FAI flakes were later washed with diethyl ether three times. Finally, the FAI flakes were dried overnight in a vacuum oven at 50 °C.

Preparation of BA/FA/Cs perovskite precursor solution. We first fabricated $FA_{0.83}Cs_{0.17}Pb(I_{0.6}Br_{0.4})_3$ precursor solution by dissolving FAI, caesium iodide (CsI; Alfa Aesar), lead iodide (PbI_2; TCI) and lead bromide ($PbBr_2$; TCI) in anhydrous *N*,*N*-dimethylformamide (DMF; Sigma-Aldrich) to obtain a stoichiometric solution. The solution was then stirred overnight in a nitrogen-filled glove box. We then added 69 µl of hydroiodic acid (HI; Sigma-Aldrich), 57 wt% in H_2O and 34.6 µl of hydrobromic acid (HBr; Sigma-Aldrich), 48 wt% in H_2O into 1 ml of 1.2 M $FA_{0.83}Cs_{0.17}Pb(I_{0.6}Br_{0.4})_3$ precursor solution, and aged the solution for approximately 48 h under a nitrogen atmosphere without stirring. In parallel, we generated $BAPb(I_{0.6}Br_{0.4})_3$ precursor solution by dissolving *n*-butylammonium iodide (BAI; Dyesol), PbI_2 and $PbBr_2$ in DMF to obtain a stoichiometric solution. The solution was also stirred overnight in a nitrogen-filled glove box. Prior to film deposition, we blended the $FA_{0.83}Cs_{0.17}Pb(I_{0.6}Br_{0.4})_3$ and $BAPb(I_{0.6}Br_{0.4})_3$ precursor solutions to achieve $BA_x(FA_{0.83}Cs_{0.17})_{1-x}Pb(I_{0.6}Br_{0.4})_3$ with desired BA contents. For $FA_{0.83}Cs_{0.17}Pb(I_{0.8}Br_{0.2})_3$ perovskite solution, we added 87.2 µl HI acid and 16.5 µl HBr acid to 1 ml of 1.2 M of the precursor solution and was aged for approximately 48 h under a nitrogen atmosphere without stirring. We then blended it with the $BAPb(I_{0.8}Br_{0.2})_3$ to achieve the $BA_x(FA_{0.83}Cs_{0.17})_{1-x}Pb(I_{0.8}Br_{0.2})_3$ precursor solution.

Substrates preparation. All of the devices were deposited on fluorine doped tin oxide (FTO)-coated glass substrates (Pilkington TEC 7). Initially, FTO was removed at specific regions for the anode contact deposition. This FTO etching was done using 2 M HCl and zinc powder. Substrates were then cleaned sequentially in Hellmanex detergent, acetone and ethanol, isopropyl alcohol, and dried with a compressed nitrogen gun. Thereafter, it was treated for 10 min in oxygen plasma.

Electron-transporting layer fabrication. Two electron-accepting layers have been discussed in this paper, as follows.

SnO_2/doped $PC_{61}BM$. Tin (IV) chloride pentahydrate ($SnCl_4 \cdot 5H_2O$) (Sigma-Aldrich) was dissolved in anhydrous 2-propanol (0.05 M) and stirred for 30 min. The solution was spin-coated at 3,000 r.p.m. for 30 s. The substrates were then dried at 100 °C for 10 min and annealed at 180 °C for 60 min. For the doped PCBM layer, we dissolved PCBM (Solenne) in anhydrous 1,2-dichlorobenzene (DCB; Sigma-Aldrich) at 10 mg ml^{-1}. We dissolved the dopant 4-(1,3-dimethyl-2,3-dihydro-1Hbenzimidazol-2-yl)-*N*,*N*-diphenylaniline (*N*-DPBI; Sigma-Aldrich) in DCB at 10 mg ml^{-1}. Both the PCBM and *N*-DPBI solutions were stirred overnight at room temperature. Prior to deposition, we added 20 µl of *N*-DPBI solution in 1 ml PCBM precursor solution. Then, we spin-coated the doped PCBM solution on top of the as-prepared SnO_2 layer in a nitrogen-filled glove box at 2,500 r.p.m. for 40 s, and annealed in nitrogen at 80 °C overnight to achieve successful doping.

SnO_2 nanoparticle/doped C_{60}. The SnO_2 nanoparticles were synthesized via a hydrothermal method, similarly to the method as previously described[48]. We dissolved 467 mg of $SnCl_4 \cdot 5H_2O$ (Sigma-Aldrich) in 20 ml of deionized water. After 10 min of stirring at room temperature, a fully dissolved, clear solution was obtained. This solution was then transferred to a Teflon-lined stainless-steel autoclave and heated for 2 h at 250 °C. After heat treatment, the autoclave was quenched to room temperature using cold water. The precipitates were centrifuged at a speed of 9,000 r.p.m. for 15 min. The nanoparticles were re-dispersed in ethanol. This washing treatment was repeated 3 times. After the final washing treatment, the nanoparticles were also re-dispersed in ethanol. On the cleaned FTO substrates, a 2 mg ml^{-1} SnO_2 nanoparticle solution was spin-coated in air at 2,000 r.p.m. for 45 s, and annealed at 150 °C for 2 min. Similar to the PCBM doping procedure, we doped the 10 mg ml^{-1} C_{60} (Solenne) precursor solution with *N*-DPBI dopant to achieve a 1 wt% *N*-DPBI/C_{60} doping ratio. The doped solution was then spin-coated on the as-prepared SnO_2 nanoparticle layer at 1,500 r.p.m. for 60 s, and annealed in nitrogen at 80 °C overnight. More details are reported elsewhere[10].

Perovskite photoactive layer fabrication. The precursor perovskite solution was spin-coated in a nitrogen-filled glove box at 2,000 r.p.m. for 45 s, on a substrate pre-heated at 80 °C. The films were dried inside the glove box on a hot plate at a temperature of 70 °C for 60 s. The films were then immediately transferred into an oven and annealed in air at 175 °C for 80 min.

Hole-transporting layer fabrication. After the perovskite films cooled down to room temperature, the 2,2′,7,7′-tetrakis[*N*,*N*-di(4-methoxyphenyl)amino]-9,9′-spirobifluorene (spiro-OMeTAD) solution was spin-coated on the perovskite layer at 2,500 r.p.m. for 40 s in a dry box (<15 RH%) as a hole-transporting layer. To obtain a spiro-OMeTAD solution, we dissolved 85.7 mg spiro-OMeTAD (Borun Technology) in 1 ml anhydrous chlorobenzene with additives of 28.8 µl *tert*-butylpyridine (*t*BP) and 20 µl lithium bis(trifluoromethylsulfonyl)imide (Li-TFSI) salt in acetonitrile (520 mg ml^{-1}). We note that the spiro-OMeTAD

layer used in the cells for stability tests was doped with 27.5 µl *tert*-butylpyridine (*t*BP) and 8.9 µl lithium bis(trifluoromethylsulfonyl)imide (Li-TFSI) salt in acetonitrile (170 mg ml^{-1}). The whole spiro-OMeTAD doping process was carried out in a nitrogen-filled glove box.

Electrode evaporation. An 80 nm gold electrode was thermally evaporated under a vacuum of $<9 \times 10^{-6}$ torr.

Current–voltage measurements. The J–V curves were measured (2400 Series SourceMeter, Keithley Instruments) under simulated AM 1.5 sunlight at 100 mW cm^{-2} irradiance generated by an Abet Class AAB sun 2,000 simulator, with the intensity calibrated with an NREL calibrated KG 5 filtered Si reference cell. The mismatch factor was calculated to be less than 1%. The active area of the solar cell is 0.0919 cm^{-2}. The forward J–V scans were measured from forward bias to short-circuit and the backward scans were from short-circuit to forward bias, both at a scan rate of 380 mV s^{-1}. A stabilization time of 10 s at forward bias of 1.4 V under illumination was performed prior to scanning.

External quantum efficiency (EQE) measurement. EQE spectra were evaluated via custom-built Fourier transform photocurrent spectroscopy based on the Bruker Vertex 80v Fourier transform spectrometer. A Newport AAA sun simulator was used as the light source and the light intensity was calibrated with a Newport-calibrated reference silicon photodiode.

Ultraviolet–visible absorption. Ultraviolet–visible absorption spectra were measured using a Bruker Vertex 80v Fourier transform infrared spectrometer fitted with a reflection/transmission accessory.

Photoluminescence spectroscopy. Photoluminescence spectra were collected with an intensified charge-coupled device (iCCD, PI-MAX4, Princeton Instruments), with each sample photoexcited by a 398 nm picosecond pulsed diode laser (PicoHarp, LDH-D-C-405M).

Scanning electron microscopy. The morphology of perovskite films was investigated using a SEM (Hitachi S-4300) at an accelerating voltage of 3–5 kV.

X-ray diffraction (XRD). The 1D- and 2D-XRD spectra of the prepared films were measured using a Rigaku SmartLab X-ray diffractometer with Cu$K_{\alpha 1}$ (1.54060 Å) and a HyPix-3000 2D hybrid pixel array detector.

Pole figure. A pole figure consists of performing a scan about the surface normal (a φ scan) with fixed 2θ, fixed ω, and at a range of ω. The surface normal is required to be a well-defined crystallographic direction (in our case [100]) and the 2θ value is set for an off-specular reflection of choice, (410). ω is set to $\omega_{410} = \theta + \Delta\theta$, where $\Delta\theta$ is equal to the angle between the [410] and specular (surface-normal, [100]) direction. One then rotates the sample about the surface normal while measuring the diffracted intensity in steps of ω about ω_{410}. In this way we can be absolutely sensitive to the in-plane orientation of the crystal structure. If a 'ring' of constant intensity is observed there is no preferential orientation within the sample plane. Conversely, if m spots (where m is the multiplicity of the measured reflection) are observed the sample is fully ordered both along the surface normal and in the sample plane (that is, epitaxial films grown on single-crystal substrates). A pole figure is of no value in a polycrystalline film as the sample scatters uniformly for all ω.

Stability test. For stability measurement, the perovskite devices were encapsulated with a hot-melt polymer foil (Oxford PV) and a glass coverslip as a barrier layer in a nitrogen-filled glove box. Before encapsulation, we blew the devices with a nitrogen gun to remove any contamination and stored them in a nitrogen-filled glove box for two days to remove any moisture residuals. All of the devices were aged under open-circuit conditions, under full-spectrum simulated AM1.5, 76 mA cm^{-2} irradiance, using an Atlas SUNTEST XLS+ (1,700 W air-cooled xenon lamp). We note that the light source is pulsed at 100 Hz frequency and we do not apply any additional ultraviolet filter during the ageing process. The chamber is air-cooled to have a temperature between 50 °C and 60 °C as indicated by a black standard temperature control unit mounted inside the ageing box. We do not have control on the humidity but monitored the laboratory humidity, which ranged from 40 to 50% relative humidity at room temperature, during the course of the ageing.

Data availability. The data that support the plots within this paper and other findings of this study are available from the corresponding author upon request.

Received 23 March 2017; accepted 14 July 2017;
published 14 August 2017

References

1. Ogomi, Y. *et al.* $CH_3NH_3Sn_xPb_{(1-x)}I_3$ perovskite solar cells covering up to 1060 nm. *J. Phys. Chem. Lett.* **5,** 1004–1011 (2014).
2. Noh, J. H., Im, S. H., Heo, J. H., Mandal, T. N. & Seok, S. Il. Chemical management for colorful, efficient, and stable inorganic-organic hybrid nanostructured solar cells. *Nano Lett.* **13,** 1764–1769 (2013).
3. Stranks, S. D. *et al.* Electron-hole diffusion lengths exceeding 1 micrometer in an organometal trihalide perovskite absorber. *Science* **342,** 341–344 (2013).
4. Oga, H., Saeki, A., Ogomi, Y., Hayase, S. & Seki, S. Improved understanding of the electronic and energetic landscapes of perovskite solar cells: high local charge carrier mobility, reduced recombination, and extremely shallow traps. *J. Am. Chem. Soc.* **136,** 13818–13825 (2014).
5. Jeon, N. J. *et al.* Solvent engineering for high-performance inorganic-organic hybrid perovskite solar cells. *Nat. Mater.* **13,** 897–903 (2014).
6. Snaith, H. J. Perovskites: the emergence of a new era for low-cost, high-efficiency solar cells. *J. Phys. Chem. Lett.* **4,** 3623–3630 (2013).
7. Yang, W. S., Park, B., Jung, E. H. & Jeon, N. J. Iodide management in formamidinium-lead-halide-based perovskite layers for efficient solar cells. *Science* **356,** 1376–1379 (2017).
8. Eperon, G. E. *et al.* Formamidinium lead trihalide: a broadly tunable perovskite for efficient planar heterojunction solar cells. *Energy Environ. Sci.* **7,** 982–988 (2014).
9. Pearson, A. J. *et al.* Oxygen degradation in mesoporous $Al_2O_3/CH_3NH_3PbI_{3-x}Cl_x$ perovskite solar cells: kinetics and mechanisms. *Adv. Energy Mater.* **6,** 1600014 (2016).
10. Wang, Z. *et al.* Efficient and air-stable mixed-cation lead mixed-halide perovskite solar cells with n-doped organic electron extraction layers. *Adv. Mater.* **29,** 1604186 (2016).
11. Aristidou, N. *et al.* The role of oxygen in the degradation of methylammonium lead trihalide perovskite photoactive layers. *Angew. Chem. Int. Edn* **54,** 8208–8212 (2015).
12. Leguy, A. M. A. *et al.* Reversible hydration of $CH_3NH_3PbI_3$ in films, single crystals, and solar cells. *Chem. Mater.* **27,** 3397–3407 (2015).
13. Conings, B. *et al.* Intrinsic thermal instability of methylammonium lead trihalide perovskite. *Adv. Energy Mater.* **5,** 1500477 (2015).
14. Misra, R. K. *et al.* Temperature- and component-dependent degradation of perovskite photovoltaic materials under concentrated sunlight. *J. Phys. Chem. Lett.* **6,** 326–330 (2015).
15. McMeekin, D. P. *et al.* A mixed-cation lead mixed-halide perovskite absorber for tandem solar cells. *Science* **351,** 151–155 (2016).
16. Yi, C. *et al.* Entropic stabilization of mixed A-cation ABX 3 metal halide perovskites for high performance perovskite solar cells. *Energy Environ. Sci.* **9,** 656–662 (2016).
17. Lee, J. W. *et al.* Formamidinium and cesium hybridization for photo- and moisture-stable perovskite solar cell. *Adv. Energy Mater.* **5,** 1501310 (2015).
18. Muljarov, E. A., Tikhodeev, S. G., Gippius, N. A. & Ishihara, T. Excitons in self-organized semiconductor/insulator superlattices: PbI-based perovskite compounds. *Phys. Rev. B* **51,** 14370–14378 (1995).
19. Stoumpos, C. C. *et al.* Ruddlesden–Popper hybrid lead iodide perovskite 2D homologous semiconductors. *Chem. Mater.* **28,** 2852–2867 (2016).
20. Smith, I. C., Hoke, E. T., Solis-Ibarra, D., McGehee, M. D. & Karunadasa, H. I. A layered hybrid perovskite solar-cell absorber with enhanced moisture stability. *Angew. Chem. Int. Edn* **53,** 11232–11235 (2014).
21. Cao, D. H., Stoumpos, C. C., Farha, O. K., Hupp, J. T. & Kanatzidis, M. G. 2D homologous perovskites as light-absorbing materials for solar cell applications. *J. Am. Chem. Soc.* **137,** 7843–7850 (2015).
22. Yao, K., Wang, X., Xu, Y. X., Li, F. & Zhou, L. Multilayered perovskite materials based on polymeric-ammonium cations for stable large-area solar cell. *Chem. Mater.* **28,** 3131–3138 (2016).
23. Tsai, H. *et al.* High-efficiency two-dimensional Ruddlesden–Popper perovskite solar cells. *Nature* **536,** 312–316 (2016).
24. Quan, L. N. *et al.* Ligand-stabilized reduced-dimensionality perovskites. *J. Am. Chem. Soc.* **138,** 2649–2655 (2016).
25. Milot, R. L. *et al.* Charge-carrier dynamics in 2D hybrid metal-halide perovskites. *Nano Lett.* **16,** 7001–7007 (2016).
26. Liao, Y. *et al.* Highly oriented low-dimensional tin halide perovskites with enhanced stability and photovoltaic performance. *J. Am. Chem. Soc.* **139,** 6693–6699 (2017).
27. Quan, L. N. *et al.* Tailoring the energy landscape in quasi-2D halide perovskites enables efficient green light emission. *Nano Lett.* **17,** 3701–3709 (2017).
28. Li, N. *et al.* Mixed cation $FA_xPEA_{1-x}PbI_3$ with enhanced phase and ambient stability toward high-performance perovskite solar cells. *Adv. Energy Mater.* **7,** 1601307 (2017).
29. He, B. B., Preckwinkel, U. & Smith, K. L. Comparison between conventional and two-dimensional XRD. *Adv. X-Ray Anal.* **46,** 37–42 (2003).

30. Tan, K. W. *et al.* Thermally induced structural evolution and performance of mesoporous block copolymer-directed alumina perovskite solar cells. *ACS Nano* **8,** 4730–4739 (2014).
31. Yuan, M. *et al.* Perovskite energy funnels for efficient light-emitting diodes. *Nat. Nanotech.* **11,** 872–877 (2016).
32. Ong, H. C., Zhu, A. X. E. & Du, G. T. Dependence of the excitonic transition energies and mosaicity on residual strain in ZnO thin films. *Appl. Phys. Lett.* **80,** 941–943 (2002).
33. Ko, H. J. *et al.* Improvement of the quality of ZnO substrates by annealing. *J. Cryst. Growth* **269,** 493–498 (2004).
34. Nagao, K. & Kagami, E. X-ray thin film measurement techniques: VII. Pole figure measurement. *Rigaku J.* **27,** 6–14 (2011).
35. Kieslich, G. *et al.* Solid-state principles applied to organic-inorganic perovskites: new tricks for an old dog. *Chem. Sci.* **5,** 4712–4715 (2014).
36. Filip, M. R., Eperon, G. E., Snaith, H. J. & Giustino, F. Steric engineering of metal-halide perovskites with tunable optical band gaps. *Nat. Commun.* **5,** 5757 (2014).
37. Safdari, M. *et al.* Layered 2D alkyldiammonium lead iodide perovskites: synthesis, characterization, and use in solar cells. *J. Mater. Chem. A* **4,** 15638–15646 (2016).
38. Morozov, S. V. *et al.* Type II-type I conversion of GaAs/GaAsSb heterostructure energy spectrum under optical pumping. *J. Appl. Phys.* **113,** 163107 (2013).
39. Van Reenen, S., Kemerink, M. & Snaith, H. J. Modeling anomalous hysteresis in perovskite solar cells. *J. Phys. Chem. Lett.* **6,** 3808–3814 (2015).
40. Belisle, R. A. *et al.* Interpretation of inverted photocurrent transients in organic lead halide perovskite solar cells: proof of the field screening by mobile ions and determination of the space charge layer widths. *Energy Environ. Sci.* **10,** 192–204 (2017).
41. Snaith, H. J. *et al.* Anomalous hysteresis in perovskite solar cells. *J. Phys. Chem. Lett.* **5,** 1511–1515 (2014).
42. Li, W. *et al.* Enhanced UV-light stability of planar heterojunction perovskite solar cells with caesium bromide interface modification. *Energy Environ. Sci.* **9,** 490–498 (2016).
43. Shao, Y., Xiao, Z., Bi, C., Yuan, Y. & Huang, J. Origin and elimination of photocurrent hysteresis by fullerene passivation in $CH_3NH_3PbI_3$ planar heterojunction solar cells. *Nat. Commun.* **5,** 5784 (2014).
44. Peters, C. H. *et al.* High efficiency polymer solar cells with long operating lifetimes. *Adv. Energy Mater.* **1,** 491–494 (2011).
45. Bush, K. A. *et al.* 23.6%-efficient monolithic perovskite/silicon tandem solar cells with improved stability. *Nat. Energy* **2,** 17009 (2017).
46. Azpiroz, J. M., Mosconi, E., Bisquert, J. & De Angelis, F. Defect migration in methylammonium lead iodide and its role in perovskite solar cell operation. *Energy Environ. Sci.* **8,** 2118–2127 (2015).
47. Wang, Q. *et al.* Scaling behavior of moisture-induced grain degradation in polycrystalline hybrid perovskite thin films. *Energy Environ. Sci.* **10,** 516–522 (2017).
48. Zhang, Y. *et al.* Two-step grain-growth kinetics of sub-7 nm SnO_2 nanocrystal under hydrothermal condition. *J. Phys. Chem. C* **119,** 19505–19512 (2015).

Acknowledgements

This work was part-funded by EPSRC, UK, the European Union Seventh Framework Program under grant agreement number 604032 of the MESO project and AFOSR through project FA9550-15-1-0115. We thank A. A. Haghighirad for discussions concerning XRD analysis, and D. P. McMeekin for discussion concerning device fabrication and film composition analysis. We would also like to thank M. T. Klug and R. Xiang for helping with illustrations.

Author contributions

H.J.S. and Z.W. conceived the project. Z.W. designed the experiments, and fabricated the devices and thin-film samples. Q.L. performed optical spectroscopy and EQE measurements and analysed the data. Z.W. and F.P.C. performed the XRD measurement and analysed the XRD data. N.S. performed SEM measurement and contributed to device fabrication. L.M.H. supervised the optical spectroscopy experiments. H.J.S. supervised the whole project. Z.W. wrote the first draft of the paper. All authors discussed the results and contributed to the writing of the paper.

Additional information

Supplementary information is available for this paper.

Reprints and permissions information is available at www.nature.com/reprints.

Correspondence and requests for materials should be addressed to H.J.S.

How to cite this article: Wang, Z. *et al.* Efficient ambient-air-stable solar cells with 2D–3D heterostructured butylammonium-caesium-formamidinium lead halide perovskites. *Nat. Energy* **2**, 17135 (2017).

Publisher's note: Springer Nature remains neutral with regard to jurisdictional claims in published maps and institutional affiliations.

Competing interests

The authors declare no competing financial interests.